Structural and Transport Properties of P2-Type Na_{0.70}Ni_{0.20}Cu_{0.15}Mn_{0.65}O₂ Layered Oxide

Hari Narayanan Vasavan, Manish Badole, Sushmita Dwivedi, and Sunil Kumar*

Department of Metallurgy Engineering and Materials Science

Indian Institute of Technology Indore, Simrol, 453552, India.

*E-mail: sunil@iiti.ac.in

Abstract

P2-type Layered oxides have attracted increasing attention recently as the cathode materials for Na-ion batteries with promising cyclability and good specific capacity. In this work, structural, electrical, and electrochemical properties of P2-type Na_{0.70}Ni_{0.20}Cu_{0.15}Mn_{0.65}O₂ (NNCM) ceramic fabricated via a sol-gel method were investigated. The Rietveld refinement of the room temperature XRD diffraction data confirmed the formation of a single P2-type phase with space group P6₃/mmc for the powder calcined at 850 °C. Complex impedance spectroscopy was used to deconvolute the contributions of grains and grain boundaries to the overall conduction inside the sample. The room temperature conductivity of the grains and grain boundaries calculated for the NNCM ceramic sintered at 950 °C were estimated to be $(5.25 \pm 0.03) \times 10^{-5} \text{ Scm}^{-1}$ and $(4.70 \pm 0.05) \times 10^{-6} \text{ Scm}^{-1}$, respectively. The respective activation energies for the grain and grain boundary conduction were 0.189 ± 0.008 eV and 0.22 ± 0.01 eV, respectively. Moreover, NNCM exhibited a sodium-ion transference number of ≈ 0.86 , suggesting that the conduction in this material is dominated by the Na-ions. The conduction mechanisms and related relaxations were also investigated using the dielectric and ac conductivity formalisms. NNCM showed specific capacities of 99 mAh/g and 74 mAh/g at 0.1C and 1C discharge rates, respectively, between 2 – 4.25 V (vs Na/Na⁺) with 95% capacity retained after 300 cycles at 1C.

Keywords: sol-gel process; X-ray methods; ionic conductivity; impedance; batteries

1. Introduction

As the world switches to greener means of energy production to tackle the issue of climate change, the availability of a cheaper and sustainable means of energy storage has become the need of the hour [1, 2]. The scarcity of lithium [3] (about 0.06% of the earth's crust), and the non-feasibility of its recycling combined with the environmental impacts of lithium mining

[4] have pushed the world to find better alternatives to Li-ion batteries. Sodium is a naturally abundant resource [3] (about 2.9% of the earth's crust), its extraction is environmentally benign, and since batteries based on Na-ions share similar manufacturing processes as that of Li-ion, these would be easier to integrate into the industrial eco-systems [5, 6]. This makes Na-ion batteries a promising alternative to lithium-ion-based energy storage systems to meet future demands [7-9]. The challenges for integrating Na-ions into batteries come from their bigger size, higher mass, and lower potential compared to Li-ion [10]. These factors would result in Na-ion batteries having lower energy capacity and poor rate performance than the conventional Li-ion batteries. Accordingly, the crystal structure, microstructure, and Na-ion dynamics inside the cell need to be optimized to ensure better electrochemical performance. Cathodes being the primary source of Na-ions in a battery predominantly determines its overall performance, and, accordingly, have been the topic of intensive research over the last decade [9].

The family of cathode materials under extensive investigation for sodium-ion batteries study can broadly be classified into 3 types: NASICON, Prussian blue, and layered oxides. NASICON stands for NA Super-Ionic CONductor, cathodes based on these materials show high voltages above 3.5 V and have good cyclabilities. Prussian blue is a novel material based on cyanides which are known to have capacities above 120 mAh/g [11]. Layered oxides are considered the most attractive cathode materials for commercial Na-ion batteries because of their higher specific capacity, cyclability, and easier synthesis compared to their competitors [12, 13]. As most of the cathode materials used in commercial Li-ion batteries are based on the same structure, certain aspects of the research and development of these materials can be translated to the advancement of Na-ion batteries. Layered oxides (LOs) based on Na have a basic formula of Na_xTMO₂; $0 \le x \le 1$, where TM is a transition metal cation or a mixture of multiple cations. These oxides are primarily found to exist in 4 phases

(named based on the nomenclature developed by Delmas *et al.* [14]) O2, O3, P2, P3. Most studies on LOs concentrate on O3 and P2 materials. P2 and P3 phases are generally found in LOs when x < 0.8 while the O3 phase has x almost equal to 1. O2, on the other hand, has x < 0.2. O3 and P2 can also reversibly transform to P3 and O2 phases, respectively, and vice versa during the de-intercalation and intercalation of Na-ions [15]. P2-type materials are seen as better electrode materials compared to O3 because of larger interlayer spacing and close-packed prismatic sites forming lower diffusion barriers leading to faster Na-ion conduction [16, 17]. O3 type layered oxides, on the other hand, have a larger concentration of Na ion, resulting in a better specific capacity.

Na_{0.67}Ni_{0.20} Cu_{0.15}Mn_{0.67}O₂, a P2 type layered oxide based on Ni and Cu, has been reported to exhibit a high capacity of 90 mAh/g with more than 80 % of capacity retained after 1000 cycles at C/10 rate [18]. Recently Na_x(Ni–Cu–Mn)O₂ system has shown an improved capacity of 120 mAh/g with an average potential of 3.4 V [19, 20]. Substituting Ni with Cu indubitably decreases specific capacity as some of the Ni²⁺/Ni³⁺ redox couples are replaced by Cu²⁺/Cu³⁺ redox couples. However, the presence of Cu²⁺ has been found to improve the structural stability of the material by preventing the ordering of Na ion vacancies which could lead to structural transformations during cycling [12, 21, 22]. For instance, P2 to O2 structural transformation is reported at 4.2 V in the undoped Na_{0.70}Ni_{1/3}Mn_{2/3}O₂ samples, while the Cu doped samples show the same transformation at 4.4 V and with improved cyclability [19-21].

The present study aims to further investigate the electrical properties of the Na_{0.70}Ni_{0.20} Cu_{0.15}Mn_{0.65}O₂ (NNCM) cathode material using impedance spectroscopy. Complex impedance spectroscopy is a versatile technique that is used to characterize a variety of materials in terms of their electrical behaviour by measuring the impedance over a wide range of frequencies, typically ranging from 10⁻² to 10⁷ Hz [23, 24]. This helps in mapping the

sample based on their electrical conduction and identifying the dominant resistive component in the sample. The contribution of the dominant conducting species towards overall conduction can then be ascertained through chronoamperometry which isolates electronic conduction from ionic conduction [25]. The information regarding the ionic conduction inside the sample is particularly important in the case of batteries employing solid electrolytes. Unlike conventional liquid electrolyte cells where the electrolyte can wet the active material particles inside the porous cathode layer and aids the ion conduction process, solid electrolytes are only in contact with the topmost particles of the cathode layer. Accordingly, much of the sodium-ion diffusion is expected to be through solids (intra- and inter-particle of active materials) [26]. Therefore, understanding the conduction mechanisms and various contributions to overall conduction becomes vital in this regard.

2. Experimental

2.1. Synthesis

Na_{0.70}Ni_{0.20}Cu_{0.15}Mn_{0.65}O₂ (NNCM) powder was synthesized through the sol-gel route. Stoichiometric amounts of nickel acetate tetrahydrate, copper (II) nitrate trihydrate, manganese (II) acetate tetrahydrate, and sodium carbonate were dissolved in distilled water and were then stirred for 5 h. Appropriate amounts of citric acid & ethylene glycol were added to the solution. The mixed solution was further stirred for another 10 h followed by heating at 100 °C to make a gel. The gel was dried at 150 °C and ground using a pestle and mortar. The resulting powder was calcinated at 550 °C for 12 h and ground again. Subsequently, the ground powder was calcined at different temperatures (700 °C, 800 °C, 850 °C, and 950 °C) for 12 h in air and cooled to room temperature in the same furnace.

2.2. Characterization

Powder X-ray diffraction (XRD) was conducted on the ground samples with a Cu- K_{α} radiation using a Bruker D2-Phaser diffractometer in 20 ranges from 10°- 70° with a step size of 0.02°. The morphology of the powder and pelletized samples was studied using a field emission scanning electron microscopy (model JEOL-7610) equipped with an energy-dispersive x-ray spectroscopy (EDS) detector.

For impedance measurements, the ground powder after calcination was pressed into a pellet and was sintered at 950 °C for 12h. The polished sample was then painted with a conductive silver paste on either side to act as the ion-blocking electrode and cured at 650 °C for 10 min. Impedance measurements were performed using a computer-controlled LCR meter (model: ZM 2376, NF Corp.) over a frequency range of 1 Hz – 1 MHz. Temperature-dependent measurements were performed using a LakeShore Cryotronics temperature controller (model: 325) between 290 – 325 K. Chronoamperometry was performed to estimate Na⁺ transference number (t_{Na}) using the Keithley Source Meter Unit (model 2450-EC) with an applied voltage of 1 V. X-ray photoelectron spectroscopy (XPS) measurements were taken using SPECS Surface Nano Analysis GmbH, Germany make spectrometer, with an Al K α X-ray source (1486.6 eV).

For electrochemical measurements, CR-2032 coin cells were fabricated with 1M NaBF₄ in tetraethylene glycol dimethyl ether (tetraglyme) as the electrolyte, Na metal as the counter electrode, and Celgard 2400 as the separator. The cathode slurry was prepared by mixing the active material, Ketjen Black, and CMC binder in DI water in the ratio 85:5:10. The slurry was then coated on an Al current collector and dried at 100 °C for 8 h in a vacuum oven. The galvanostatic charge-discharge tests were carried out using a Landt battery testing system (LANHE CT, 2001A)

3. Results and Discussion

3.1. Structural properties

Figure 1 shows the phase evolution of NNCM with calcination temperature. P2 materials show their strongest peak at $\sim 15.8^{\circ}$. The presence of this peak in the XRD pattern for the sample calcined at 550 °C indicates the presence of a P2 phase in the sample along with other peaks corresponding to unreacted precursors & intermediate phases. At higher calcination temperatures intensity of the peaks related to P2 is observed to increase while peaks corresponding to other impurity phases disappear. A single P2-type phase is obtained for the sample calcined at 850 °C. Two minor peaks in the vicinity of $2\theta \approx 28^{\circ}$ in the XRD pattern for this sample (denoted by *) suggest the ordering of Na⁺ vacancies in Na_{0.70}Ni_{0.20}Cu_{0.15}Mn_{0.65}O₂ [27-29].

Rietveld refinement of the room temperature x-ray diffraction data for the sample sintered at 950 °C was carried out using the software package TOPAS Academic (version 6) [30]. Refinement profile, as shown in Fig. 2, confirms a single P2 phase based on a hexagonal symmetry with P63/mmc space group for NNCM. A low-intensity peak observed at $\sim 39^{\circ}$ suggests the presence of minor CuO impurities. The fraction of this impurity was estimated to be less than 1 % of the sample. The difference between the calculated and observed data is plotted as a dark grey line at the bottom in Fig. 2. The low intensity of the difference profile along with small values of reliability factors (GOF = 1.77, R_{WP} = 19.2, R_P = 15.1, and R_{EXP} = 10.8) suggest the high accuracy of the refined crystal structure parameters and the choice of structure model. The lattice parameters for the hexagonal unit cell obtained after refinement were $a = 2.8896 \pm 0.0007$ Å, and $c = 11.1803 \pm 0.0005$ Å. The cell volume V was calculated to be 81.850 ± 0.005 Å³. These values concur with the data reported in the literature for other P2-type layered oxides such as $Na_{0.75}Cu_{0.15}Ni_{0.20}Mn_{0.65}O_2$ (a = 2.887 Å, c = 11.078 Å), $Na_{0.75}Cu_{0.33}Mn_{0.77}O_2$ (a = 2.850 Å, c = 11.188 Å), $Na_{2/3}Ni_{1/3}Mn_{5/9}Al_{1/9}O_2$ (a = 2.869 Å, c = 11.124 Å), etc. [18, 20, 22, 31]. The crystallographic unit cell of the P2-type layered oxide

based on the data from Rietveld refinement of the XRD pattern (see Table 1) is shown in Fig. 3. Software package VESTA was used to generate these images [32]. The volume of TM - O_6 octahedron for NNCM is calculated to be 9.678 Å³, whereas the Na - O_6 prism volume is \sim 12.958Å³. The area of the square bottleneck for the sodium intercalation at the Na-1 site (Fig. 3) is \sim 10.353 Å². Na-O and effective TM-O bond lengths are 2.448 \pm 0.005 Å and 1.947 \pm 0.004 Å, respectively.

The SEM image of the powder sample calcined at 850 °C is shown in Fig. 4(a). The powdered sample shows hexagonal plates with well-defined facets indicating good crystallinity (Fig. 4(a)). The particles were observed to have an average size of 1.9 μ m \pm 0.4 μ m and an average thickness of about 0.25 μ m. This corresponds to a typical aspect ratio of ~ 8. The (100), (010), (110), ($\bar{1}00$), (0 $\bar{1}0$), ($\bar{1}\bar{1}0$) planes in NNCM hexagonal lattice have higher surface energies as compared {001} planes. Accordingly, the equilibrium shape of the NNCM crystal as predicted by Wulff plots is hexagon-type flakes with dominant {001} surfaces. The cross-sectional SEM image of fractured surface of pellet sintered at 950 °C for 12 h (Fig. 4(b)) exhibits randomly oriented and tightly packed grains. The calculated relative density of the pellet was ~ 90 \pm 2 %. Elemental mapping performed using EDS (shown in Fig. 4(c)) points to a uniform distribution of Na, Ni, Mn, Cu, and O elements throughout the sample. The segregation of Cu seen in Fig. 4(c1) is due to minor CuO impurities in the sample.

3.2. XPS

The oxidation states of the transition metals in NNCM were verified using X-ray photoelectron spectroscopy. The XPS spectra of Mn-2p, Ni-2p, Cu-2p, and Na-1s are displayed in Fig. 5. In the Mn-2p spectra, the peaks centred at 643 eV (Mn $2p_{3/2}$) and ~ 654 eV (Mn- $2p_{1/2}$) confirm the existence Mn⁴⁺ ions in the samples [33, 34]. The four

characteristic peaks in the Ni-2p and Cu-2p spectra are attributed to Ni-2p_{3/2} (\sim 855 eV), Ni-2p_{1/2} (\sim 872 eV), Cu-2p_{3/2} (\sim 933 eV) and Cu-2p_{1/2} (\sim 953 eV) and their respective shake-up satellite peaks indicating that Ni and Cu maintained a +2 oxidation state in the sample [33, 34]. In the Na spectrum, the peak at \sim 1071 eV indicating the 1+ oxidation state of Na ions [33, 34], is quite broad and can be deconvoluted into 2 peaks pertaining to 2 different crystallographic sites for Na in the NNCM unit cell [18].

3.3. Electrical properties

To study the transport behaviour of NNCM, temperature-dependent impedance measurements were performed on the pelletised sample sintered at 950 °C for 12 h. Nyquist plots (-Z" versus Z') plotted at various temperatures in the 300 - 325 K range are shown in Fig. 6. The plots show two semi-circular arcs at higher and intermediate frequencies, which are typically attributed to the contributions of grain and grain boundary towards overall impedance in the material. The third linear tail component seen at lower frequencies is due to sodium-ion blocking at the silver electrodes which suggests substantial ionic conduction in NNCM. With the increase in temperature, the intercepts of the semi-circular arc on the x-axis shift towards lower values (Figs. 6(a) & 6(b)). To deconvolute the contributions from grains, grain boundaries, and sample-electrode interface, the impedance is usually analyzed through equivalent circuit modeling. Equivalent circuits consist of a combination of resistive elements (R), inductors (L), and reactive elements such as capacitors (C) or constant phase elements (CPE) connected in series or parallel [23, 24, 35, 36]. Each component in the circuit is representative of a different physical process inside the sample [24]. CPEs are regarded as leaky capacitors or capacitors with a resistive component and represent deviations from an ideal capacitive behavior [37-40]. The impedance of the constant phase element is given by

$$Z_{CPE}^* = \frac{1}{A(j\omega)^n} \tag{1}$$

Where A and n are constants and $j = \sqrt{-1}$. 'n' in formula 1 varies between 0 and 1 with 0 representing a pure resistor and 1 an ideal capacitor.

The equivalent circuit shown as the inset of Fig. 6(c) was employed to analyze the impedance data for NNCM. The fitted values of circuit elements R1, R2, CPE1, CPE2, and CPE3 (Table 3) confirmed that the large semi-circle seen in the Nyquist plots with large capacitive and resistance values corresponds to grain boundaries. The poorly resolved arc in higher frequency regions arises from grains. Therefore, the parallel combination of R1 and CPE1 in the model represents the grains, R2 & CPE2 (Table 2) represent the highly resistive grain boundaries, and the element CPE3 represents the highly capacitive sample-electrode interface region. Further, the values of n associated with the element CPE1 was ~ 0.97 , and that for the element CPE2 was ~ 0.5 at all temperatures. This indicate that the conductivity relaxation in the grains has a comparatively much lesser deviation from the ideal Debye behaviour than that in grain boundary regions [40].

The values of room temperature DC conductivity of the grains and grain boundaries were calculated using the fitted values of R1, R2 and sample dimensions ($\sigma = t/(R \times A)$; t is the thickness of pellet and A is the area of cross-section of the pellet) and were found to be about $(5.25 \pm 0.05) \times 10^{-5} \text{ Scm}^{-1}$ and $(4.70 \pm 0.03) \times 10^{-6} \text{ Scm}^{-1}$, respectively. The total conductivity of the sample was calculated to be about $(4.28 \pm 0.08) \times 10^{-6} \text{ Scm}^{-1}$. The DC conductivities of both grains and grain boundaries are temperature-dependent and show an increasing trend with the increase in temperature. Activation energies (E_A) for grain and grain boundary regions, temperature-dependent conductivity values were fitted using the Arrhenius equation.

$$\sigma(T) = \sigma_0 \ e^{-(\frac{E_A}{kT})} \tag{2}$$

where σ_{θ} is the pre-exponential factor, k is Boltzmann's constant, and T is the absolute temperature (Fig. 7). All three DC conductivities (grain conductivity σ_{G} , grain boundary σ_{GB} and total conductivity σ_{total}) show an almost linear trend in the Arrhenius plot confirming that the conduction process in NNCM is thermally activated. The RT values of activation energies along with the diffusion coefficients (D) estimated using the Nernst Einstein relation (eq. 3) are provided in Table 3.

$$D = \frac{kT}{Nq^2} \sigma_{DC} \tag{3}$$

Where N is the number density of charge carriers per unit volume of the unit cell and q is the elementary charge. The diffusion coefficients calculated through the galvanostatic intermittent titration technique (GITT) for different P2 type cathodes reported in the literature are shown in Table 4.

To confirm the ion conduction indicated by the tail component in the Nyquist plots, chronoamperometry was performed on the sample at room temperature under an applied DC voltage of 1 V. As displayed in Fig. 8, the initial value of the current (I_0) is around 126.6 μ A and a steady current close to 16.6 μ A is recorded after the exponential decay. While the initial current (I_0) is attributed to the movement of Na-ions and electrons through the sample, only the latter contributes to the steady-state current (I_{ss}) due to the Na-ions being blocked at the silver electrodes [25, 38]. The Na⁺ transference number (I_{Na}) estimated using the formula $I_{Na} = (I_0 - I_{ss})/I_0$ is about 0.86. Such a high value of ion transference number coupled with the high value of room temperature conductivity (of order I_0 S/cm) in grain region indicates facile sodium ion conduction in NNCM crystal structure. The room temperature grain electronic conductivity of NNCM is estimated to be about I_0 S/cm.

To further elucidate the relaxations associated with the Na-ions in NNCM, frequency variation of real and imaginary parts of dielectric permittivity (calculated using equations (5) and (6) was studied.

$$\varepsilon^* = \varepsilon' - j\varepsilon$$
 (4)

$$\varepsilon' = \frac{Z''}{\omega C_0 (Z'^2 + Z''^2)} \tag{5}$$

$$\varepsilon'' = \frac{Z'}{\omega C_0(Z'^2 + Z''^2)} \tag{6}$$

Where ε' and ε'' are the real and imaginary parts of the dielectric permittivity, $j = \sqrt{-1}$, ω $(2\pi f)$ is the angular frequency and C_0 is the capacitance of the sample. ε' is representative of the capacitance and polarization in the sample while ε'' indicates dielectric loss and conductance within the sample [47]. The loss tangent (tan δ), given by ϵ''/ϵ' and the real part σ' (= $\omega \epsilon_0 \epsilon''$) of the complex ionic conductivity have also been calculated and plotted against frequency (f) as shown in Fig. 9 (b). At 1 Hz, both ε' and ε'' (Fig. 9 (a), at 300 K) show a value close to 10⁸ which decreases exponentially with the increase in frequency. The high dielectric constant values at low frequencies are indicative of high space-charge polarization caused by the blocking of Na-ions at the sample - electrode interface [48]. The slope of ε'' versus f curve is almost equal to -1 at low and intermediate frequencies which suggests a high dc conduction through the sample [47, 49]. Further evidence for both the electrode polarization and dc conduction can be seen in the σ' versus f plot (Fig. 9(b)). The decrease in ac conductivity values in the low-frequency regime (shown as 1) is attributed to the electrode polarization [49]. The deviation observed from the above-discussed trend in both the ε' versus f and ε'' versus f curves at frequencies above 10⁴ Hz is due to relaxation of Na⁺ ions in the grains which normally occurs at high frequencies due to their low resistance towards electrical conduction [23]. Typically, such relaxation causes step-like drop in the ε' versus

frequency plot centered around a characteristic relaxation frequency which is accompanied with a peak in ε'' versus frequency plot at the same relaxation frequency. In NNCM, dominating effects of high values of dc conductivity and a strong electrode polarisation, especially at lower frequencies, suppress the grain boundaries relaxation related features in frequency variation of the dielectric permittivity. Accordingly, no peaks in ε'' versus frequency plot are apparent in Fig. 9. However, the peaks relating to grain (depicted as B in Fig. 9 (b)) and grain boundary (depicted as A) relaxations are clearly observed in the tan δ versus f curve in high and low frequencies regions, respectively [50].

3.4. Electrochemical properties

The galvanostatic charge/discharge (GCD) profiles of the NNCM cathode cycled between 2.00 – 4.25 V (vs. Na/Na⁺) at discharge rates of 0.1C, 0.2C, and 1C are displayed in Fig. 10 (a). At a discharge rate of 0.1C, the sample showed a specific capacity of 99 mAh/g, which decreased to 74 mAh/g at 1C. All the profiles show a decreased slope between 3 – 4 V, while a higher slope is observed between 2 – 3 V. This is because the Ni^{2+/4+} and Cu^{2+/3+} redox couples are active between 3 – 4 V; hence the cell shows most of its capacity in this voltage range [51, 52]. In terms of cyclic performance, the cell retained 95% of its initial capacity after 300 cycles when cycled at 1C (Fig. 10(b)), making it an attractive material as cathode for Na-ion batteries for long-term stationary storage applications.

4. Conclusions

In summary, Na_{0.70}Ni_{0.20}Cu_{0.15}Mn_{0.65}O₂ was successfully synthesized using a sol-gel route. Rietveld refinement of the powder XRD data shows a single P2 phase with a hexagonal lattice (P6₃/mmc space group). SEM analysis of the powder sample shows hexagon-like plates with an average particle size of $\sim 2.14 \ \mu m$. Elemental mapping confirmed the uniform distribution of the constituent elements throughout the sample. Impedance measurements

suggest the conductivity of Na-ions in NNCM ceramics is greatly influenced by the highly resistive grain boundaries. The conductivity of grain boundaries was found to be about 4.7×10^{-6} Scm⁻¹ while that of the grains was around 5.25×10^{-5} Scm⁻¹ at room temperature. The values of activation energies (E_A) were found to be 0.22 ± 0.01 eV for grain boundary conduction, 0.189 ± 0.008 eV for grain conduction, and 0.21 ± 0.01 eV for overall conduction in NNCM ceramic sample. Chronoamperometry and dielectric response establish the dominance of Na-ions in the overall conduction of this material. The material showed a specific capacity of 99 mAh/g and 74 mAh/g at 0.1C and 1C, respectively, with 95% of its initial capacity retained after 300 cycles at 1C.

Acknowledgements

SK acknowledges the Scientific and Engineering Research Board (SERB) for the Core Research Award (Grant number: CRG/ 2021/005548). Authors thank UGC-DAE CSR, Indore, and Dr. Uday Deshpande for providing XPS measurements.

References

- [1] P. Denholm, E. Ela, B. Kirby, M. Milligan, The Role of Energy Storage with Renewable Electricity Generation, (2010) https://doi.org/10.2172/972169
- [2] I. Aşchilean, N. Cobîrzan, A. Bolboaca, R. Boieru, R.-A. Felseghi, Pairing solar power to sustainable energy storage solutions within a residential building: A case study, International Journal of Energy Research, 45 (2021) 15495-15511 https://doi.org/10.1002/er.6982
- [3] Mineral commodity summaries 2021, Mineral Commodity SummariesReston, VA, 2021, pp. 200.

- [4] D.B. Agusdinata, W. Liu, H. Eakin, H. Romero, Socio-environmental impacts of lithium mineral extraction: towards a research agenda, Environmental Research Letters, 13 (2018) 123001 https://doi.org/10.1088/1748-9326/aae9b1
- [5] C. Vaalma, D. Buchholz, M. Weil, S. Passerini, A cost and resource analysis of sodiumion batteries, Nature Reviews Materials, 3 (2018) 18013 https://doi.org/10.1038/natrevmats.2018.13
- [6] J. Peters, A. Cruz, M. Weil, Exploring the Economic Potential of Sodium-Ion Batteries, Batteries, 5 (2019) 10 https://doi.org/10.3390/batteries5010010
- [7] D. Buchholz, A. Moretti, R. Schmuch, S. Nowak, S. V, W. M, S. Passerini, Towards Naion batteries Synthesis and Characterization of a novel high capacity Na-ion intercalation material, ChemInform, 160 (2013) 44 https://doi.org/10.1002/chin.201319014
- [8] Y.E. Durmus, H. Zhang, F. Baakes, G. Desmaizieres, H. Hayun, L. Yang, M. Kolek, V. Küpers, J. Janek, D. Mandler, S. Passerini, Y. Ein-Eli, Side by Side Battery Technologies with Lithium-Ion Based Batteries, Advanced Energy Materials, 10 (2020) 2000089 https://doi.org/10.1002/aenm.202000089
- [9] L. Qiao, X. Judez, T. Rojo, M. Armand, H. Zhang, Review—Polymer Electrolytes for Sodium Batteries, J. Electrochem. Soc., 167 (2020) 070534 10.1149/1945-7111/ab7aa0
- [10] Z. Liu, X. Xu, S. Ji, L. Zeng, D. Zhang, J. Liu, Recent Progress of P2-Type Layered Transition-Metal Oxide Cathodes for Sodium-Ion Batteries, Chemistry – A European Journal, 26 (2020) 7747-7766 https://doi.org/10.1002/chem.201905131
- [11] R. Usiskin, Y. Lu, J. Popovic, M. Law, P. Balaya, Y.-S. Hu, J. Maier, Fundamentals, status and promise of sodium-based batteries, Nature Reviews Materials, 6 (2021) 1020-1035 https://doi.org/10.1038/s41578-021-00324-w

- [12] J. Darga, J. Lamb, A. Manthiram, Industrialization of Layered Oxide Cathodes for Lithium-Ion and Sodium-Ion Batteries: A Comparative Perspective, Energy Technology, 8 (2020) 2000723 https://doi.org/10.1002/ente.202000723
- [13] R.J. Clément, P.G. Bruce, C.P. Grey, Review—Manganese-Based P2-Type Transition Metal Oxides as Sodium-Ion Battery Cathode Materials, Journal of The Electrochemical Society, 162 (2015) A2589-A2604 https://doi.org/10.1149/2.0201514jes
- [14] C. Delmas, C. Fouassier, P. Hagenmuller, Structural classification and properties of the layered oxides, Physica B+C, 99 (1980) 81-85 https://doi.org/10.1016/0378-4363(80)90214-4
- [15] C. Zhao, Z. Yao, Q. Wang, H. Li, J. Wang, M. Liu, S. Ganapathy, Y. Lu, J. Cabana, B. Li, X. Bai, A. Aspuru-Guzik, M. Wagemaker, L. Chen, Y.-S. Hu, Revealing High Na-Content P2-Type Layered Oxides as Advanced Sodium-Ion Cathodes, Journal of the American Chemical Society, 142 (2020) 5742-5750 https://doi.org/10.1021/jacs.9b13572
- [16] S. Guo, Y. Sun, J. Yi, K. Zhu, P. Liu, Y. Zhu, G.-z. Zhu, M. Chen, M. Ishida, H. Zhou, Understanding sodium-ion diffusion in layered P2 and P3 oxides via experiments and first-principles calculations: a bridge between crystal structure and electrochemical performance, NPG Asia Materials, 8 (2016) e266-e266 https://doi.org/10.1038/am.2016.53
- [17] J. Liu, W.H. Kan, C.D. Ling, Insights into the high voltage layered oxide cathode materials in sodium-ion batteries: Structural evolution and anion redox, Journal of Power Sources, 481 (2021) 229139 https://doi.org/10.1016/j.jpowsour.2020.229139
- [18] W. Kang, D.Y.W. Yu, P.-K. Lee, Z. Zhang, H. Bian, W. Li, T.-W. Ng, W. Zhang, C.-S. Lee, P2-Type Na_xCu_{0.15}Ni_{0.20}Mn_{0.65}O₂ Cathodes with High Voltage for High-Power and Long-Life Sodium-Ion Batteries, ACS Applied Materials & Interfaces, 8 (2016) 31661-31668 https://doi.org/10.1021/acsami.6b10841

- [19] L. Yang, S.-h. Luo, Y. Wang, Y. Zhan, Q. Wang, Y. Zhang, X. Liu, W. Mu, F. Teng, Cu-doped layered P2-type Na_{0.67}Ni_{0.33-x}Cu_xMn_{0.67}O₂ cathode electrode material with enhanced electrochemical performance for sodium-ion batteries, Chemical Engineering Journal, 404 (2020) 126578 https://doi.org/10.1016/j.cej.2020.126578
- [20] L. Wang, Y.-G. Sun, L.-L. Hu, J.-Y. Piao, J. Guo, A. Manthiram, J. Ma, A.-M. Cao, Copper-substituted Na_{0.67}Ni_{0.3-x}Cu_xMn_{0.7}O₂ cathode materials for sodium-ion batteries with suppressed P2–O2 phase transition, Journal of Materials Chemistry A, 5 (2017) 8752-8761 https://doi.org/10.1039/C7TA00880E
- [21] J. Xu, J. Chen, K. Zhang, N. Li, L. Tao, C.-P. Wong, Na_x(Cu–Fe–Mn)O₂ system as cathode materials for Na-ion batteries, Nano Energy, 78 (2020) 105142 https://doi.org/10.1016/j.nanoen.2020.105142
- [22] W. Kang, Z. Zhang, P.-K. Lee, T.-W. Ng, W. Li, Y. Tang, W. Zhang, C.-S. Lee, D.Y. Wai Yu, Copper substituted P2-type Na_{0.67}Cu_xMn_{1-x}O₂: a stable high-power sodium-ion battery cathode, Journal of Materials Chemistry A, 3 (2015) 22846-22852 https://doi.org/10.1039/C5TA06371J
- [23] D.C. Sinclair, A.R. West, Impedance and modulus spectroscopy of semiconducting BaTiO₃ showing positive temperature coefficient of resistance, Journal of Applied Physics, 66 (1989) 3850-3856 https://doi.org/10.1063/1.344049
- [24] J.T.S. Irvine, D.C. Sinclair, A.R. West, Electroceramics: Characterization by Impedance Spectroscopy, Advanced Materials, 2 (1990) 132-138 https://doi.org/10.1002/adma.19900020304
- [25] T. Pareek, S. Dwivedi, S.A. Ahmad, M. Badole, S. Kumar, Effect of NASICON-type LiSnZr(PO₄)₃ ceramic filler on the ionic conductivity and electrochemical behavior of PVDF

based composite electrolyte, Journal of Alloys and Compounds, 824 (2020) 153991 https://doi.org/10.1016/j.jallcom.2020.153991

- [26] M. Hahn, D. Rosenbach, A. Krimalowski, T. Nazarenus, R. Moos, M. Thelakkat, M.A. Danzer, Investigating solid polymer and ceramic electrolytes for lithium-ion batteries by means of an extended Distribution of Relaxation Times analysis, Electrochimica Acta, 344 (2020) 136060 https://doi.org/10.1016/j.electacta.2020.136060
- [27] P.-F. Wang, H.-R. Yao, X.-Y. Liu, Y.-X. Yin, J.-N. Zhang, Y. Wen, X. Yu, L. Gu, Y.-G. Guo, Na⁺ vacancy disordering promises high-rate Na-ion batteries, Science Advances, 4 (2018) eaar6018 https://doi.org/10.1126/sciadv.aar6018
- [28] D.H. Lee, J. Xu, Y.S. Meng, An advanced cathode for Na-ion batteries with high rate and excellent structural stability, Physical Chemistry Chemical Physics, 15 (2013) 3304-3312 https://doi.org/10.1039/C2CP44467D
- [29] R. Berthelot, D. Carlier, C. Delmas, Electrochemical investigation of the P2–Na_xCoO₂ phase diagram, Nature Materials, 10 (2011) 74-80 https://doi.org/10.1038/nmat2920
- [30] A. Coelho, TOPAS and TOPAS-Academic: an optimization program integrating computer algebra and crystallographic objects written in C++, Journal of Applied Crystallography, 51 (2018) 210-218 https://doi.org/10.1107/S1600576718000183
- [31] X.-H. Zhang, W.-L. Pang, F. Wan, J.-Z. Guo, H.-Y. Lü, J.-Y. Li, Y.-M. Xing, J.-P. Zhang, X.-L. Wu, P2–Na_{2/3}Ni_{1/3}Mn_{5/9}Al_{1/9}O₂ microparticles as superior cathode material for sodium-ion batteries: enhanced properties and mechanism via graphene connection, ACS applied materials & interfaces, 8 (2016) 20650-20659

https://doi.org/10.1021/acs.chemmater.5b04557

- [32] K. Momma, F. Izumi, VESTA 3 for three-dimensional visualization of crystal, volumetric and morphology data, Journal of Applied Crystallography, 44 (2011) 1272-1276 https://doi.org/10.1107/S0021889811038970
- [33] J.F. Moulder, J. Chastain, Handbook of X-ray Photoelectron Spectroscopy: A Reference Book of Standard Spectra for Identification and Interpretation of XPS Data, Physical Electronics Division, Perkin-Elmer Corporation1992.
- [34] S. Hüfner, Photoelectron spectroscopy: principles and applications, Springer Science & Business Media 2013.
- [35] A.R.C. Bredar, A.L. Chown, A.R. Burton, B.H. Farnum, Electrochemical Impedance Spectroscopy of Metal Oxide Electrodes for Energy Applications, ACS Applied Energy Materials, 3 (2020) 66-98 https://doi.org/10.1021/acsaem.9b01965
- [36] W. Woodward, Broadband Dielectric Spectroscopy—A Practical Guide, 2021, pp. 3-59.
- [37] L.A. Middlemiss, A.J.R. Rennie, R. Sayers, A.R. West, Characterisation of batteries by electrochemical impedance spectroscopy, Energy Reports, 6 (2020) 232-241 https://doi.org/10.1016/j.egyr.2020.03.029
- [38] S. Kumar, K.B.R. Varma, Influence of lanthanum doping on the dielectric, ferroelectric and relaxor behaviour of barium bismuth titanate ceramics, Journal of Physics D: Applied Physics, 42 (2009) 075405 https://doi.org/10.1088/0022-3727/42/7/075405
- [39] M.A. Hernández, N. Masó, A.R. West, On the correct choice of equivalent circuit for fitting bulk impedance data of ionic/electronic conductors, Applied Physics Letters, 108 (2016) 152901 https://doi.org/10.1063/1.4946008
- [40] E. von Hauff, Impedance Spectroscopy for Emerging Photovoltaics, Journal of Physical Chemistry C, 123 (2019) 11329-11346 https://doi.org/10.1021/acs.jpcc.9b00892

- [41] Z.-Y. Li, R. Gao, L. Sun, Z. Hu, X. Liu, Designing an advanced P2-Na_{0.67}Mn_{0.65}Ni_{0.2}Co_{0.15}O₂ layered cathode material for Na-ion batteries, Journal of Materials Chemistry A, 3 (2015) 16272-16278 https://doi.org/10.1039/C5TA02450A
- [42] N. Bucher, S. Hartung, J.B. Franklin, A.M. Wise, L.Y. Lim, H.-Y. Chen, J.N. Weker, M.F. Toney, M. Srinivasan, P2–Na_xCo_yMn_{1-y} O₂ (y= 0, 0.1) as Cathode Materials in Sodium-Ion Batteries Effects of Doping and Morphology To Enhance Cycling Stability, Chemistry of Materials, 28 (2016) 2041-2051 https://doi.org/10.1021/acs.chemmater.5b04557
- [43] Z.-Y. Li, J. Zhang, R. Gao, H. Zhang, L. Zheng, Z. Hu, X. Liu, Li-Substituted Co-Free Layered P2/O3 Biphasic Na_{0.67}Mn_{0.55}Ni_{0.25}Ti_{0.2-x}Li_xO₂ as High-Rate-Capability Cathode Materials for Sodium Ion Batteries, The Journal of Physical Chemistry C, 120 (2016) 9007-9016 https://doi.org/10.1021/acs.jpcc.5b11983
- [44] L.A. Ma, R. Palm, E. Nocerino, O.K. Forslund, N. Matsubara, S. Cottrell, K. Yokoyama, A. Koda, J. Sugiyama, Y. Sassa, M. Månsson, R. Younesi, Na-ion mobility in P2-type $Na_{0.5}Mg_xNi_{0.17-x}Mn_{0.83}O_2\ (0 \le x \le 0.07)\ from\ electrochemical\ and\ muon\ spin\ relaxation$ studies, Physical Chemistry Chemical Physics, 23 (2021) 24478-24486 https://doi.org/10.1039/D1CP03115E
- [45] N.A. Katcho, J. Carrasco, D. Saurel, E. Gonzalo, M. Han, F. Aguesse, T. Rojo, Origins of Bistability and Na Ion Mobility Difference in P2-and O3-Na_{2/3}Fe_{2/3}Mn_{1/3}O₂ Cathode Polymorphs, Advanced Energy Materials, 7 (2017) 1601477 https://doi.org/10.1002/aenm.201601477
- [46] L. Zheng, J. Li, M. Obrovac, Crystal structures and electrochemical performance of air-stable Na_{2/3}Ni_{1/3-x} Cu _x Mn_{2/3}O₂ in sodium cells, Chemistry of Materials, 29 (2017) 1623-1631 https://doi.org/10.1021/acs.chemmater.6b04769

- [47] Y. Huang, K. Wu, Z. Xing, C. Zhang, X. Hu, P. Guo, J. Zhang, J. Li, Understanding the validity of impedance and modulus spectroscopy on exploring electrical heterogeneity in dielectric ceramics, Journal of Applied Physics, 125 (2019) 084103 https://doi.org/10.1063/1.5081842
- [48] S. Kumar, K.B.R. Varma, Dielectric relaxation in bismuth layer-structured BaBi₄Ti₄O₁₅ ferroelectric ceramics, Current Applied Physics, 11 (2011) 203-210 https://doi.org/10.1016/j.cap.2010.07.008
- [49] S. Corezzi, S. Capaccioli, G. Gallone, M. Lucchesi, P.A. Rolla, Dynamics of a glass-forming triepoxide studied by dielectric spectroscopy, Journal of Physics: Condensed Matter, 11 (1999) 10297-10314 https://doi.org/10.1088/0953-8984/11/50/322
- [50] D.M. Abdel-Basset, S. Mulmi, M.S. El-Bana, S.S. Fouad, V. Thangadurai, Structure, Ionic Conductivity, and Dielectric Properties of Li-Rich Garnet-type $\text{Li}_{5+2x}\text{La}_3\text{Ta}_{2-x}\text{Sm}_x\text{O}_{12}$ (0 \leq x \leq 0.55) and Their Chemical Stability, Inorganic Chemistry, 56 (2017) 8865-8877 https://doi.org/10.1021/acs.inorgchem.7b00816
- [51] K. Tang, Y. Huang, X. Xie, S. Cao, L. Liu, H. Liu, Z. Luo, Y. Wang, B. Chang, H. Shu, X. Wang, Electrochemical performance and structural stability of air-stable
 Na_{0.67}Ni_{0.33}Mn_{0.67-x}Ti_xO₂ cathode materials for high-performance sodium-ion batteries,
 Chemical Engineering Journal, 399 (2020) 125725 https://doi.org/10.1016/j.cej.2020.125725
- [52] Q. Pei, M. Lu, Z. Liu, D. Li, X. Rao, X. Liu, S. Zhong, Improving the Na_{0.67}Ni_{0.33}Mn_{0.67}O₂ Cathode Material for High-Voltage Cyclability via Ti/Cu Codoping for Sodium-Ion Batteries, ACS Applied Energy Materials, 5 (2022) 1953-1962 https://doi.org/10.1021/acsaem.1c03466

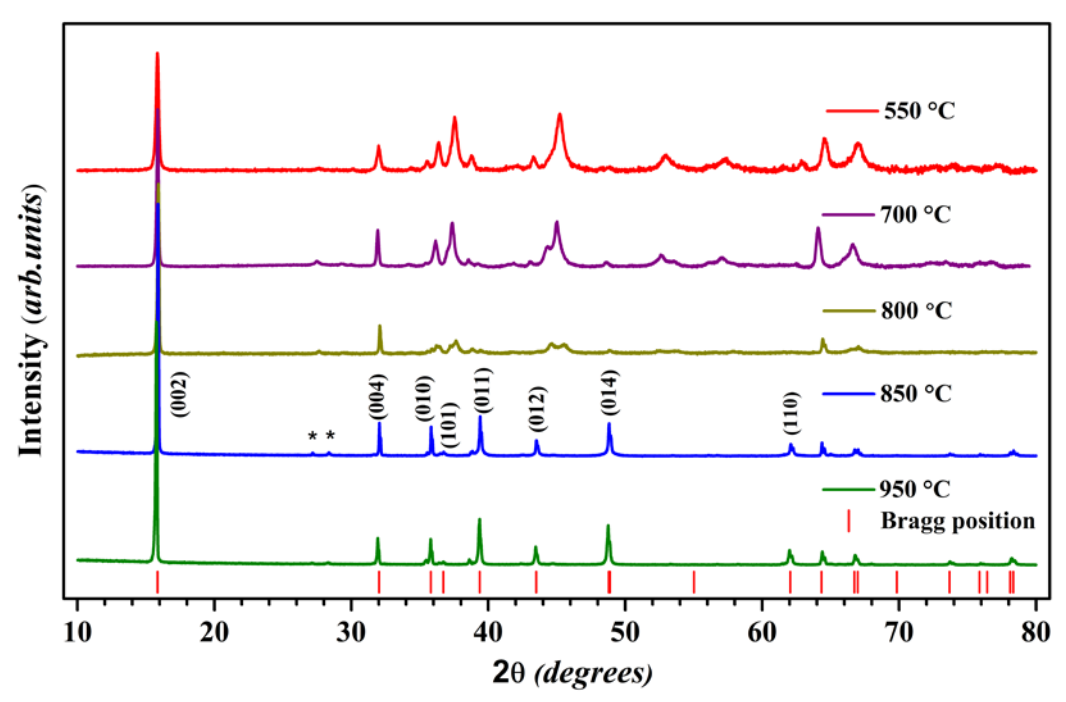


Figure 1. XRD patterns of NNCM samples calcined at different temperatures. The * symbol indicates peaks related to superlattice reflections caused by Na⁺ vacancy ordering.

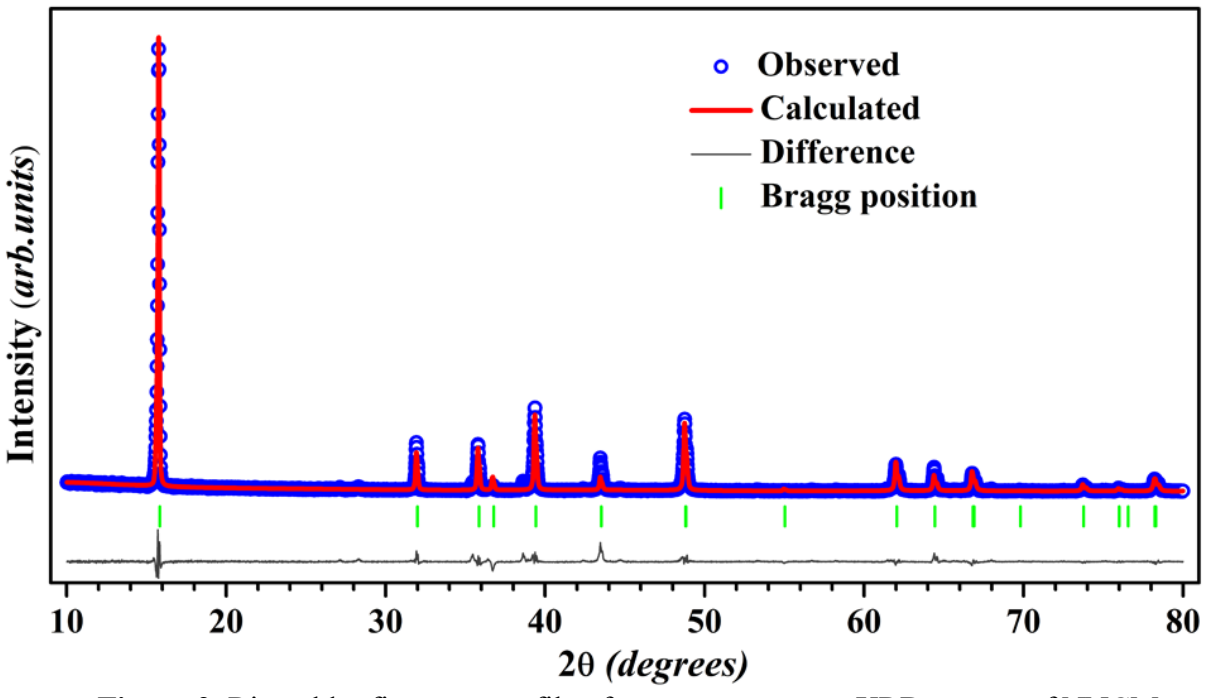


Figure 2. Rietveld refinement profile of room temperature XRD pattern of NNCM sample sintered at 950 °C for 12 h.

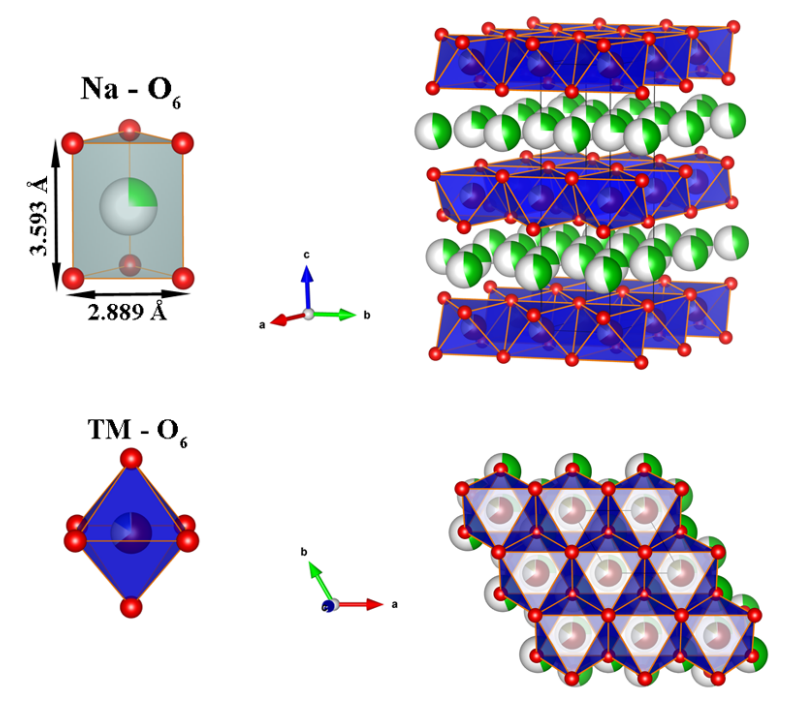


Figure 3. Crystal structure of P2 type - NNCM sample visualized using VESTA.

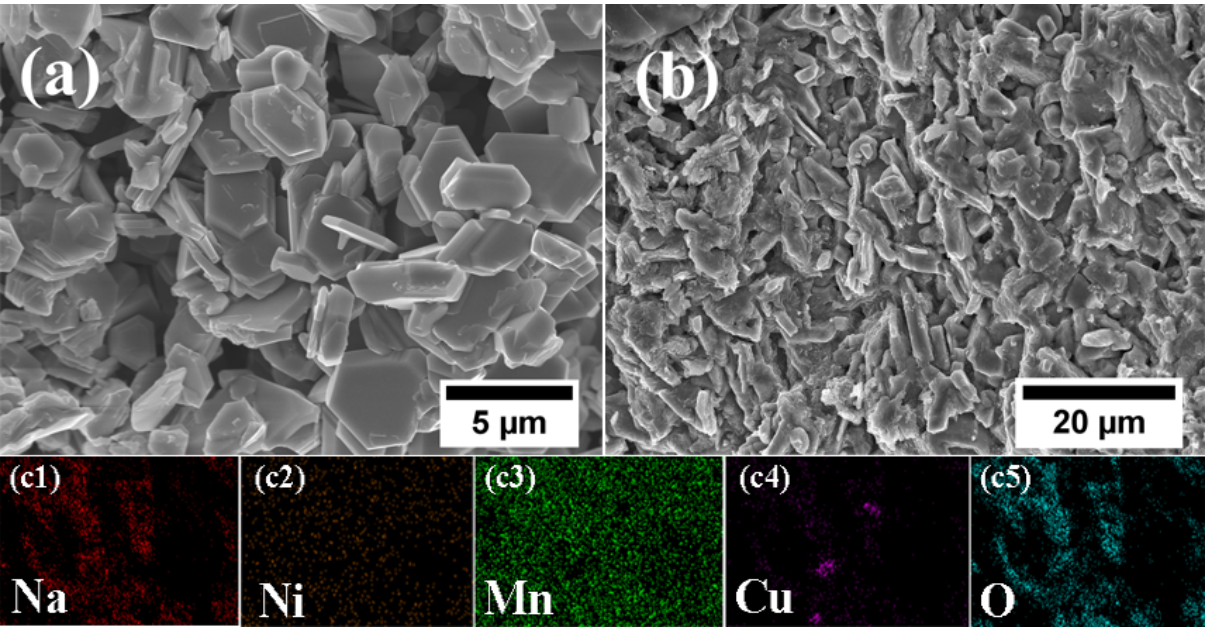


Figure 4. SEM image of NNCM (a) powder calcined at 850 °C (b) fractured surface of the pellet sintered at 950 °C (c) EDS maps of (c1) Na, (c2) Ni, (c3) Mn, (c4) Cu, and (c5) O for the sample surfaces shown in (b).

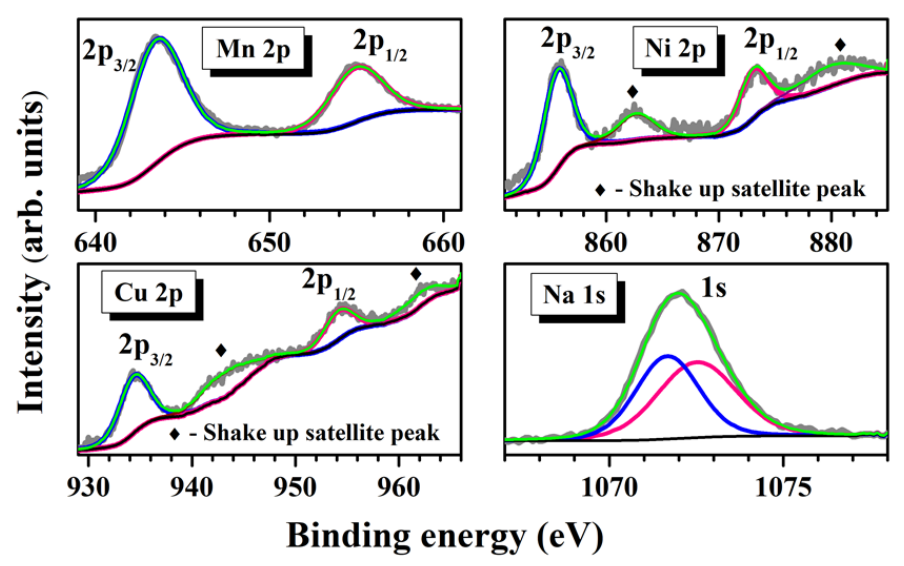


Figure 5. XPS spectra of as prepared NNCM sample.

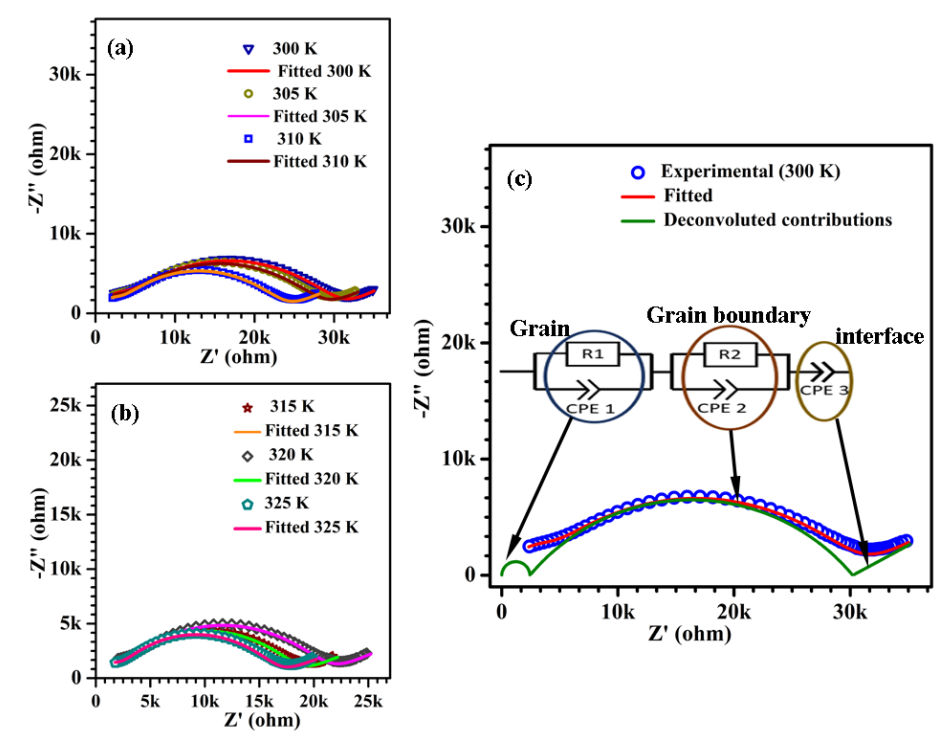


Figure 6. Nyquist plots of NNCM at different temperatures: (a) 300-310 K, (b) 315-325 K, and (c) 300 K. The impedance data was fitted using the equivalent circuit shown in Fig. 6(c) inset. The deconvoluted contributions of grain, grain boundary, and electrode interface to total impedance are depicted by the solid green line in Fig. 6(c).

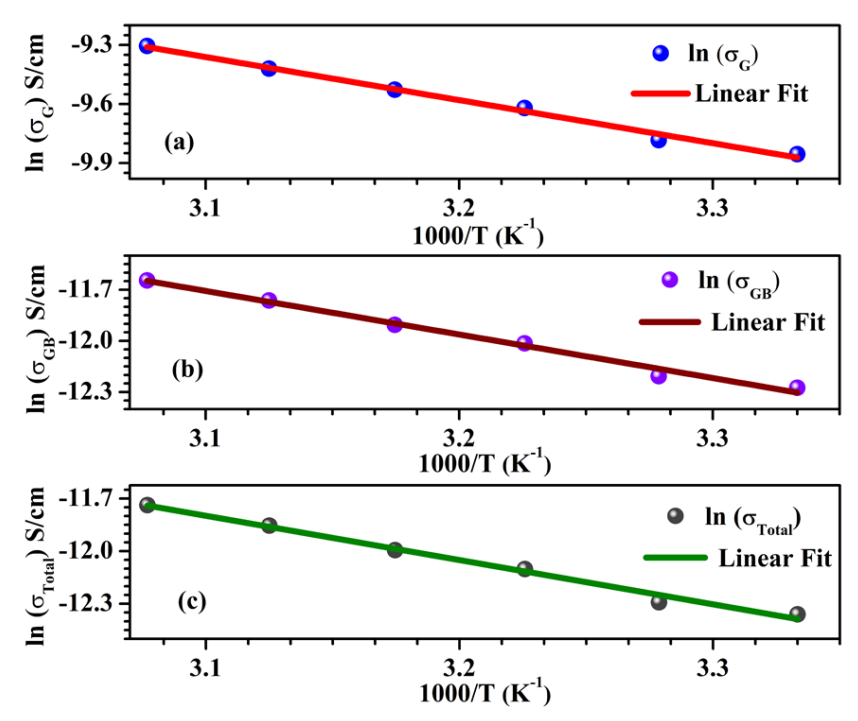


Figure 7. Arrhenius plots showing temperature dependence of (a) grain conductivity σ_G (b) grain boundary conductivity σ_{GB} , and (c) total conductivity σ_{total} .

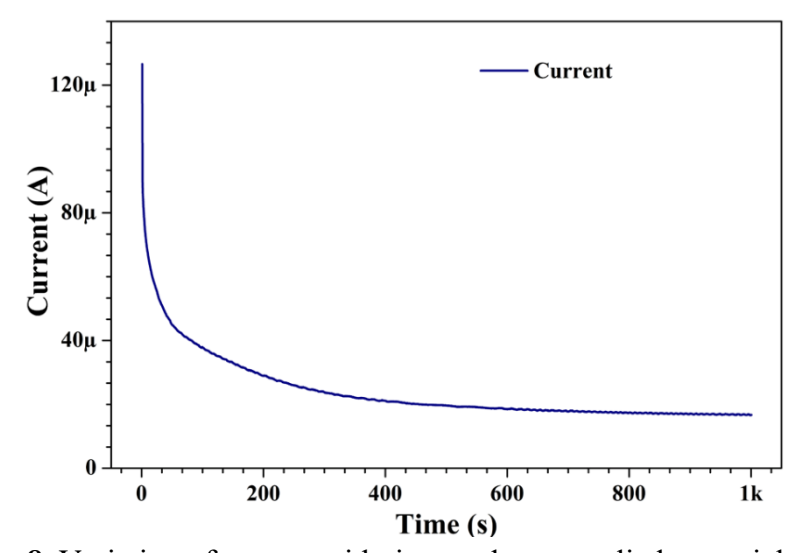


Figure 8. Variation of current with time under an applied potential of 1 V.

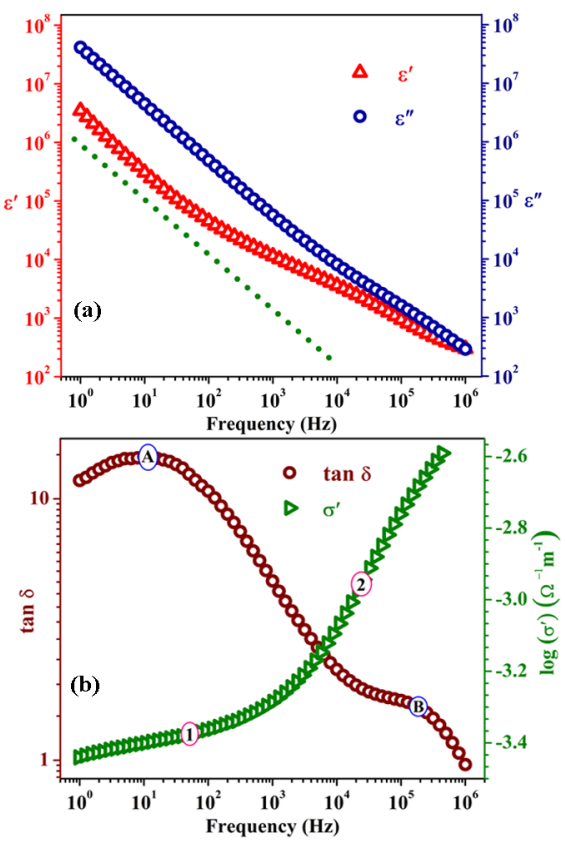


Figure 9. (a) ε' and ε'' versus frequency plot at 300 K. The dotted line represents a slope of -1 (b) Conductivity (σ') and tan δ versus frequency plots at 300 K.

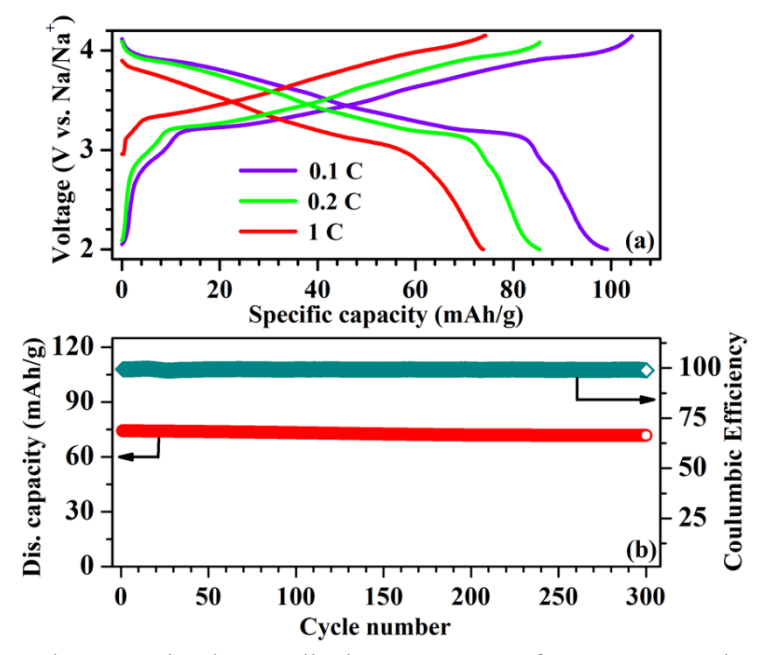


Figure 10. (a) Galvanostatic charge-discharge curves of NNCM samples at discharge rates of 0.1C, 0.2C and 1C. (b) Cyclic performance of the NNCM samples at 1C for 300 cycles.

Table. 1. Crystallographic parameters of P2-type NNMC obtained from Rietveld refinement of room temperature XRD data.

Atom	X	y	z	Occupancy	Site
Na1	2/3	1/3	1/4	0.45	2d
Na2	0	0	1/4	0.25	2b
Mn/ Ni/ Cu	0	0	0	0.65/0.20/0.15	2a
0	2/3	1/3	0.089	1	4f

Table. 2. Parameters obtained after fitting the impedance data of NNMC at 300 K.

Component	Resistance (in Ω)	C for CPE (in F)	n for CPE
Grain	2425	1.00×10^{-10}	0.97
Grain Boundary	27790	9.96 × 10 ⁻⁸	0.55
Interface	-	1.00×10^{-4}	0.31

Table 3. DC conductivities, activation energies, and diffusion coefficients of grain, grain boundary, and overall sample (total) at room temperature (300 K).

Component	DC Conductivity (Scm ⁻¹)	Activation Energy (eV)	Diffusion Coefficient (m ² s ⁻¹)
Grain	$(5.25 \pm 0.05) \times 10^{-5}$	0.189 ± 0.008	4.91×10^{-14}
Grain Boundary	$(4.70 \pm 0.03) \times 10^{-6}$	0.22 ± 0.01	4.39×10^{-15}
Total	$(4.28 \pm 0.08) \times 10^{-6}$	0.21 ± 0.01	4.00×10^{-15}

Table 4. Na⁺ diffusion coefficients in various P2 type layered oxides.

Compound	Diffusion Coefficient (m ² s ⁻¹)	Ref.
Na _{0.67} Mn _{0.65} Ni _{0.2} Co _{0.15} O ₂	1.0 ×10 ⁻¹⁸	[41]
Na _{0.6} Co _{0.1} Mn _{0.9} O ₂	1 ×10 ⁻¹⁷	[42]

$Na_{0.67}Mn_{0.55}Ni_{0.25}Li_{0.2}O_2$	9.81×10^{-18}	[43]
$Na_{2/3}Ni_{1/3}Mn_{5/9}Al_{1/9}O_2$	2.5×10^{-16}	[31]
$Na_{0.5}Mg_{0.02}Ni_{0.15}Mn_{0.83}O_2$	5.4×10^{-14}	[44]
$Na_{2/3}Fe_{2/3}Mn_{1/3}O_2$	1.3×10^{-16}	[45]
$Na_{2/3}Cu_{1/12}Ni_{1/4}Mn_{2/3}O_2$	1.0×10^{-16}	[46]
$Na_{0.70}Ni_{0.20}Cu_{0.15}Mn_{0.65}O_{2} \\$	4.9×10^{-14}	This work